ACS central science

http://pubs.acs.org/journal/acscii

Research Article

Solvent Gaming Chemistry to Control the Quality of Halide Perovskite Thin Films for Photovoltaics

Xiaofeng Huang,[‖] Guocheng Deng,[‖] Shaoqi Zhan,[‖] Fang Cao, Fangwen Cheng, Jun Yin, Jing Li, Binghui Wu,* and Nanfeng Zheng*

Cite This: *ACS Cent. Sci.* 2022, 8, 1008−1016

Read Online

ACCESS | Metrics & More | Article Recommendations | Supporting Information

ABSTRACT: Research on solvent chemistry, particularly for halide perovskite intermediates, has been advancing the development of perovskite solar cells (PSCs) toward commercial applications. A predictive understanding of solvent effects on the perovskite formation is thus essential. This work systematically discloses the relationship among the basicity of solvents, solvent-contained intermediate structures, and intermediate-to-perovskite α-$FAPbI_3$ evolutions. Depending on their basicity, solvents exhibit their own favorite bonding selection with FA^+ or Pb^{2+} cations by forming either hydrogen bonds or coordination bonds, resulting in two different kinds of intermediate structures. While both intermediates can be evolved into α-$FAPbI_3$ below the δ-to-α thermodynamic temperature, the hydrogen-bond-favorable kind could form defect-less α-$FAPbI_3$ via sidestepping the break of strong coordination bonds. The disclosed solvent gaming mechanism guides the solvent selection for fabricating high-quality perovskite films and thus high-performance PSCs and modules.

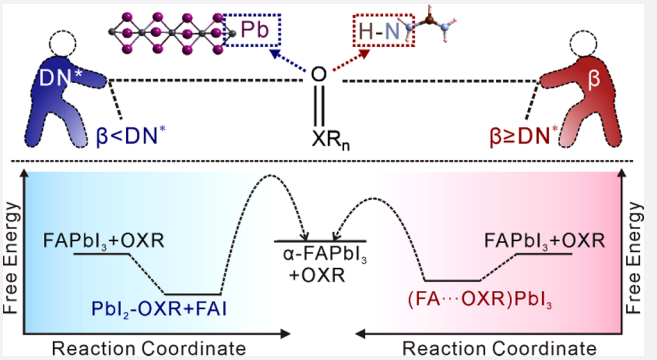

INTRODUCTION

Solvents play essential roles in chemical, physical, and biological processes.[1−5] A deep understanding of solvent chemistry is beneficial to the development of solution-processed material systems and their devices. For example, in-depth solvent chemistry studies of electrolytes within Li ion batteries help to improve the performance and boost the industrialization process of energy storage.[6,7] Similarly, solvent chemistry cannot be overemphasized in the recently emerging system of solution-processed organic−inorganic halide perovskites (OIHPs).[8−12] The ABX_3 structure of OIHPs is composed of a three-dimensional network of corner-shared BX_6 octahedra and A^+ counter cations situated in the voids.[13] With the ability to bind to the precursors of OIHPs, Lewis basic solvent molecules [e.g., dimethyl sulfoxide (DMSO), *N*-methylpyrrolidone (NMP), and *N*,*N*-dimethylformamide (DMF)] play critical roles in regulating the perovskite film crystallization from solution phase to achieve a high power conversion efficiency of the resulting perovskite solar cells (PSCs) over 25%.[14−19] A comprehensive understanding of solvent effects is thus highly needed for the preparation of high-quality OIHP films, which is still, however, far from being satisfactory and complete.

Among various OIHPs, formamidine lead iodide ($FAPbI_3$) has been proven as an ideal candidate for high-performance PSCs,[20−25] and the critical Lewis basic solvent molecules work through solution-processed $FAPbI_3$ formation, sequentially referring to the chemical origin of the intermediate structure, crystallization kinetics, and structural evolution of the intermediate-to-perovskite phase transition.[26,27] According to the Lewis acid−base theory, while cationic FA^+ and Pb^{2+} sites with Lewis acidic properties have different trends of combining with Lewis basic solvents to form various intermediate structures,[28,29] such as PbI_2−DMF, PbI_2−NMP, and (FA···DMF)PbI_3, predictively regulating $FAPbI_3$-based intermediate structures from different solvent molecules is still unrevealed at present.[30] In addition, the $FAPbI_3$ structure commonly processes two totally different phases, including 3C α-$FAPbI_3$ ($P3m1$ space group) with corner-shared PbI_6 octahedra and 2H δ-$FAPbI_3$ ($P6_3mc$ space group) with face-shared PbI_6 octahedra. The photoinactive δ-$FAPbI_3$ phase requires a high transition energy (e.g., annealing at 150 °C) to be reconstructed into the photoactive α-$FAPbI_3$ phase.[31−33] Although the final perovskite formation would be tremendously determined by intermediate structures,[34−38] a principal explanation on intermediate-involved α-$FAPbI_3$ growth is still lacking.[39,40] Hence, revealing chemical principles of inter-

Received: April 2, 2022
Published: July 19, 2022

https://doi.org/10.1021/acscentsci.2c00385
ACS Cent. Sci. 2022, 8, 1008−1016

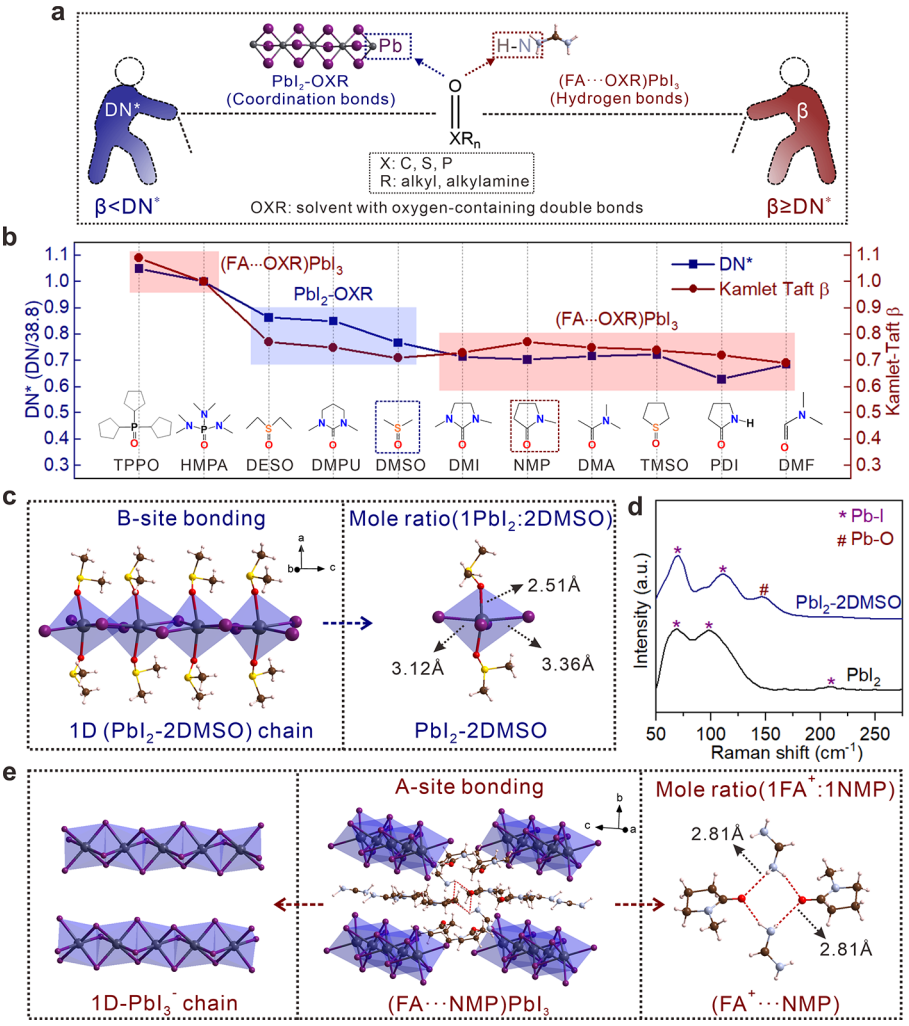

Figure 1. Inductive formation rule of PbI_2−OXR or (FA···OXR)PbI_3 structures. (a) Solvent gaming scheme and two interaction types between Lewis acidic FA^+/Pb^{2+} cations and Lewis basic OXRs, depending on the solvent basicity in terms of DN* and Kamlet−Taft β values. Color legend: dark gray, Pb; plum, I; brown, C; ice-blue, N; hermosa pink, H. (b) Summary of solvent gaming results and as-formed intermediate structures. When β < DN*, PbI_2−OXR forms; when $\beta \geq$ DN*, (FA···OXR)PbI_3 emerges from $FAPbI_3$-based solutions. The mole ratio of Pb and OXR is omitted here, and dashed boxes show the examples studied in details *infra*. Molecular abbreviation: tris(*N*,*N*-tetramethylene) phosphoric acid triamide, TPPO; hexamethyl phosphoryl triamide, HMPA; diethyl sulfoxide, DESO; *N*,*N*-dimethylpropyleneurea, DMPU; 1,3-dimethyl-2-imidazolidinone, DMI; *N*,*N*-dimethylacetamide, DMA; tetramethylene sulfoxide, TMSO; 2-pyrrolidinone, PDI. (c) Crystal structure of PbI_2−2DMSO. (d) Demonstration of the Pb−O bond within the PbI_2−2DMSO structure by Raman spectra. (e) Crystal structure of (FA···NMP)PbI_3.

mediate structures behind the solvent dependence would further highly advance the rational growth of α-$FAPbI_3$ films toward high-performance devices.

In this work, we report that the solvent-contained $FAPbI_3$-based intermediate structures are classified and correlated to the basicity of solvents. Two related physicochemical parameters of solvent basicity, the Gutmann donor number (DN) and Kamlet−Taft β value, are demonstrated to show a competitive selection to determine the structures of solvent-contained intermediates: when $\beta \geq$ DN* (DN* = DN/38.8), solvents integrate with FA^+ cations to form hydrogen bonds within the (FA···solvent)PbI_3 lattice; when β < DN*, solvents coordinate with Pb^{2+} to form the PbI_2−solvent lattice, but FA^+ cations are excluded. Subsequently, the different intermediate structures based on solvent gaming directly affect the thermodynamics and kinetics of α-$FAPbI_3$ formation; while both intermediates (e.g., (FA···NMP)PbI_3 and PbI_2−2DMSO + FAI) can transfer into α-$FAPbI_3$ below the thermodynamic temperature of the traditional δ-to-α phase transition, it is found that the hydrogen-bond-favorable intermediates ($\beta \geq$ DN*) sidestep the breaking of strong coordination bonds and assist the formation of defect-less α-$FAPbI_3$ films. The revealed solvent gaming mechanism provides a rational guide toward high-performance PSCs with enhanced stability.

■ RESULTS AND DISCUSSION

In this work, the widely used O-donors, Lewis basic solvents with similar oxygen-containing double bonds (abbreviated as OXRs: X, C, S, and P; R, alkyl and alkylamine), are the main focus. It should be noted that the basicity of OXRs can be commonly evaluated by DN[41,42] and β values.[43,44] The higher the DN, the stronger the coordination ability; high-DN OXRs are expected to combine Pb^{2+} cations to form strong coordination bonds. Similarly, the higher the β, the stronger the hydrogen-bonding interaction; hydrogen bonds should be easily formed between FA^+ cations and high-β OXRs.[45,46] Common OXRs used for the preparation of $FAPbI_3$-based solutions are selected in this work, and their DN and β values

https://doi.org/10.1021/acscentsci.2c00385
ACS Cent. Sci. 2022, 8, 1008−1016

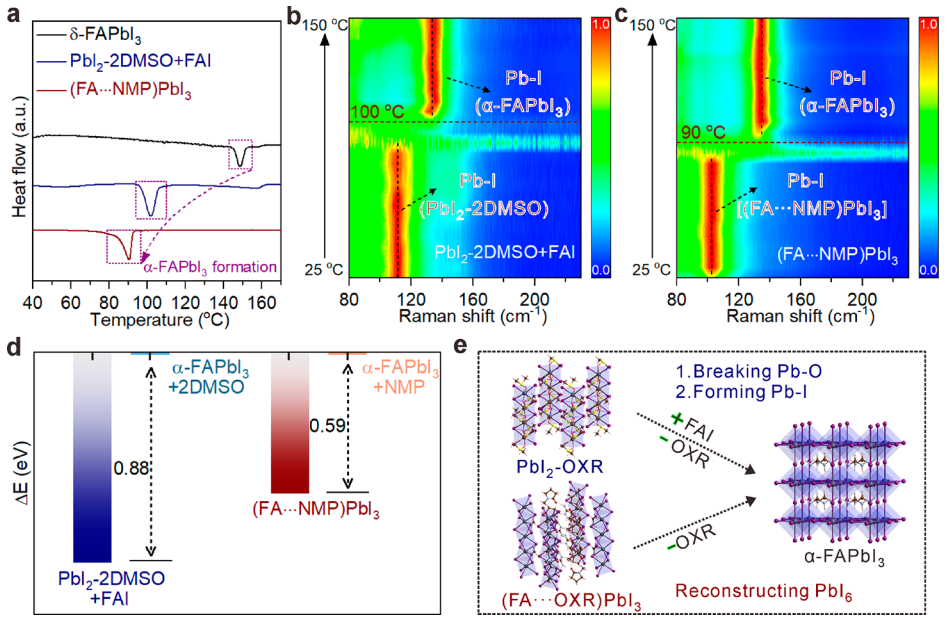

Figure 2. Structural evolution from two types of intermediate structures to α-$FAPbI_3$. (a) DSC curves of $(FA\cdots NMP)PbI_3$, PbI_2−2DMSO + FAI (grinding mixture), and δ-$FAPbI_3$ powders. *In situ* temperature-dependent Raman spectra of (b) PbI_2−2DMSO + FAI (grinding mixture) and (c) $(FA\cdots NMP)PbI_3$. α-$FAPbI_3$ formation from PbI_2−OXR (with FAI addition) or $(FA\cdots OXR)PbI_3$ to α-$FAPbI_3$ referring to (d) DFT calculations and (e) structural evolutions. Color legend: dark gray, Pb; plum, I; red, O; yellow, S; brown, C; ice-blue, N; hermosa pink, H.

are adopted from the previous literature or measured results (Figure S1 and Tables S1−S3). While there is a positive relationship among DN and β values, the different measurement methods limit the direct comparison of these two parameters of Lewis basicities. For a straightforward comparison, the DN value of hexamethyl phosphoryl triamide (HMPA, whose DN and β are 38.8 kcal/mol and 1.0, respectively) was used as a reference to give a normalized DN* (defined as DN/38.8) for predicting the chemical interaction of OXRs with Lewis acids. Such interaction between FA^+/Pb^{2+} and OXRs behind solvent gaming chemistry is predicted to result in two types of intermediate structures, i.e., PbI_2−OXR and $(FA^+\cdots OXR)PbI_3$, depending on the DN* and β relative values of OXRs (Figure 1a).

As expected, the PbI_2−OXR intermediates were easily formed from the solutions containing PbI_2 and OXRs, confirmed by the XRD data (Figure S2). However, the competition among FA^+/Pb^{2+} cations and OXRs takes place in the copresence of FA^+ and Pb^{2+} cations (i.e., $FAPbI_3$ + OXRs solutions). Compared to pure OXR, the introduction of FAI or PbI_2 into OXR can trigger the shift of ^{16}O NMR (Figure S3), demonstrating that the existence of $FA^+\cdots OXR$ or Pb^{2+}−OXR interaction in the solution phase. However, during the growth of intermediate crystals from the solutions, the dynamic equilibrium between two interactions would be broken, resulting in final crystal structures with the thermodynamically most stable state. Therefore, the solvent gaming phenomenon forming Pb^{2+}−OXR or $FA^+\cdots OXR$ couples was observed: while PbI_2−OXR intermediates grew in the case of β < DN*, another kind of $(FA\cdots OXR)PbI_3$ intermediates were disclosed for the OXRs with $\beta \geq$ DN*. Thus, an inductive formation rule is described in Figure 1b: (1) OXRs with β < DN* tend to strongly coordinate with Pb^{2+} to form B-site intermediates (i.e., PbI_2−OXR); (2) OXRs with $\beta \geq$ DN* weaken the coordination interaction with Pb^{2+} and enhance the hydrogen bonding with FA^+ to form A-site intermediates [i.e., $(FA\cdots OXR)PbI_3$]. Note that the simultaneous presence of $FA^+\cdots OXR$ and Pb^{2+}−OXR couples was not revealed in the obtained intermediate structures. Combining the two physicochemical parameters of solvent basicity should help to predict the gaming results for forming either PbI_2−OXR or $(FA\cdots OXR)PbI_3$ intermediates.

The molecular structures of most of the above intermediates were determined by single crystal X-ray analysis and classified into two types (Figures S4 and S5; see detailed parameters of crystals in Tables S4 and S5). In the following discussion, two commonly used solvents with different basicity types, DMSO (β < DN*) and NMP (β > DN*) for the preparation of α-$FAPbI_3$, are chosen as examples to differentiate their intrinsic structures in detail. The PbI_2−2DMSO crystal consists of one-dimensional single chains made of edge-shared PbI_4O_2 octahedra (Figure 1c). While two DMSO molecules occupy the unshared vertices of each octahedron via the Pb—O coordination, four I^- vertices are coordinated and shared by each neighboring octahedron. The strong Pb—O coordination bond (2.51 Å) between DMSO and Pb^{2+} cations excludes FA^+ as part of the PbI_2−2DMSO structure and was identified by the Pb—O Raman characteristic peak at 150 cm^{-1} (Figure 1d). By contrast, the $(FA\cdots NMP)PbI_3$ crystal consists of one-dimensional PbI_3^- chains with face-shared PbI_6 octahedra. The void space among the PbI_3^- chains is occupied by an equimolar ratio of FA^+ counter cations and NMP molecules (Figure 1e). Note that the $(FA\cdots NMP)PbI_3$ intermediate displays a similar structure, Pb—I vibration, and optical absorption (Figure S6) to δ-$FAPbI_3$.[31] No Pb—O signal is observed in $(FA\cdots NMP)PbI_3$, except for the enlarged cells due to the intercalated NMP molecules. In addition, the observed short distance of ~2.81 Å between the N atom (from —N—H of FA^+) and O atom (from —C═O of NMP) implies the existence of $FA^+\cdots NMP$ hydrogen bonds. The attenuated total internal reflectance Fourier transform infrared spectra (ATR-FTIR) and room-temperature and temperature-dependent ^1H

https://doi.org/10.1021/acscentsci.2c00385
ACS Cent. Sci. 2022, 8, 1008−1016

NMR characterizations (Figure S7) of (FA···NMP)PbI_3 demonstrated that the formation of —N—H···O═C— is key to the stable NMP intercalation in the as-formed (FA···NMP)PbI_3 lattice at room temperature.

The structural evolution of the intermediate-to-perovskite phase transition is sequentially studied. The δ- to α-$FAPbI_3$ transition at only 77 °C has been proven to be theoretically thermodynamics-favorable[33] but experimentally dynamics-unfavorable.[31] The two above-mentioned solvent-contained intermediates with different chemical bonding types provide a rational guide for in-depth studies of their α-$FAPbI_3$ formation pathways. Note that PbI_2−2DMSO needs to be mixed with equimolar FAI for its α-$FAPbI_3$ formation. Experimentally, differential scanning calorimetry (DSC) curves in Figure 2a show that, for the α-$FAPbI_3$ formation routes from PbI_2−2DMSO + FAI (grinding mixture) and (FA···NMP)PbI_3 powders, similar endothermic peaks appeared below 150 °C compared to those from δ-$FAPbI_3$, and (FA···NMP)PbI_3 has a slightly lower α-$FAPbI_3$ formation temperature (90 °C) than the case of PbI_2−2DMSO + FAI (100 °C). As revealed by *in situ* Raman characterizations (Figure 2b,c and Figure S8a,b), both cases of PbI_2−2DMSO + FAI (grinding mixture) and (FA···NMP)PbI_3 display an obvious disappearance of the Pb−I vibration (110 and 103 cm^{-1}, belonging to respective Pb−I polyhedra) and appearance of the α-$FAPbI_3$ characteristic vibration at 135 cm^{-1} around 90−100 °C, demonstrating their α-$FAPbI_3$ formation below the thermodynamic temperature of the δ-to-α transition (i.e., 150 °C; Figure S8c). Different behaviors toward α-$FAPbI_3$ might imply different structural evolutions and were experimentally revealed. While the pure PbI_2−2DMSO crystals exhibited a strong (110) diffraction peak, PbI_2−2DMSO + FAI (grinding mixture) showed a decreased crystallinity (Figure S8d). When one PbI_2−2DMSO crystal was attached by FAI and subjected to heating at 100 °C, the interface gradually changed from yellow to orange and finally black (Figure S9). The remaining part of the PbI_2−2DMSO crystal only changed to yellow due to its partial decomposition. The DSC data from the sample by simply mixing PbI_2−2DMSO + FAI powders (without grinding) displays two endothermic peaks: the low-temperature peak corresponds to α-$FAPbI_3$ formation, and the high-temperature one corresponds to PbI_2−2DMSO decomposition (Figure S10a−c). The decreased temperature of α-$FAPbI_3$ formation from PbI_2−2DMSO + FAI is similar to the reported result that the expanded (001) distance between adjacent I−Pb−I sandwiches promoted the kinetic process of PbI_6 octahedra reconstitution.[47] In the (FA···NMP)PbI_3 case, the thermogravimetric analysis and *in situ* ATR-FTIR determined the dissociation temperature of NMP molecules from (FA···NMP)PbI_3 lattices (Figure S10d−f). Single crystal XRD patterns of a (FA···NMP)PbI_3 crystal before and after heating at 90 °C confirmed that driving out NMP from the (FA···NMP)PbI_3 lattice directly triggered α-$FAPbI_3$ formation. In comparison, δ-$FAPbI_3$ only turned black at 150 °C (Figure S11).

Density functional theory (DFT) calculations (Figure 2d) further revealed that the conversion from (FA···NMP)PbI_3 to α-$FAPbI_3$ + NMP required 0.59 eV for each unit cell, lower energy input than α-$FAPbI_3$ + 2DMSO from PbI_2−2DMSO + FAI (0.88 eV; Table S6). The slight difference in formation energy is consistent with the above thermodynamic trend (Figure 2a−c). A transition-state structure of face-shared PbI_6 octahedra (abbreviated as the meta-phase) was built by removing all of the NMP molecules from the (FA···NMP)PbI_3 lattice (Figure S12a). The energy difference among the meta-phase and α-phase was calculated to be only 0.18 eV; the *ab initio* molecular dynamics further confirmed that the meta-phase structure gradually connected with adjacent ones by a corner-shared mode of the I-vertex and exhibited the favorable conversion trend to corner-shared ones of α-$FAPbI_3$ at 90 °C (Figure S12b). Hence, both intermediates favor the α-$FAPbI_3$ formation in terms of similar thermodynamic states but undergo totally different kinetic structural evolutions. Generally, α-$FAPbI_3$ from PbI_2−OXR + FAI involves the breakage of Pb−O bonds, reformation of Pb−I bonds, intercalation of FA^+ counter cations, and reconstruction of PbI_6 octahedra behind thermodynamic behaviors. In contrast, removing OXRs from the (FA···OXR)PbI_3 lattice directly triggers the α-$FAPbI_3$ formation (Figure 2e). Both PbI_2−OXR (with FAI addition) and (FA···OXR)PbI_3 structures, including PbI_2−DMPU, (FA···2DMF)PbI_3, (FA···2.5DMI)PbI_3, (FA···0.5DMA)PbI_3, and (FA···HMPA)PbI_3, demonstrated thermodynamic behaviors similar to those of the respective PbI_2−2DMSO and (FA···NMP)PbI_3 (Figure S13). More interestingly, ethyl acetate, used as an antisolvent to extract OXRs from (FA···OXR)PbI_3, could promote the rapid formation of black α-$FAPbI_3$ at room temperature (Figure S14a−c). However, a similar phenomenon was not observed in the PbI_2−OXR + FAI case, due to the hindered kinetic behaviors simultaneously referring to OXR dissociation, FAI intercalation, and structural reconstruction (Figure S14d). These results identify that the two intermediate structures with different solvent-binding modes differentiate the thermodynamic and kinetic pathways of α-$FAPbI_3$ formation, explaining the decreased temperature required for α-$FAPbI_3$ formation by solvent-atmosphere treatment.[48] In short, the relationships among the basicity of OXRs, $FAPbI_3$-based intermediate structures, and α-$FAPbI_3$ formation pathways have been successfully built. The altered α-$FAPbI_3$ formation pathways would affect the quality of perovskite films.[49,50]

Starting from (FA···NMP)PbI_3 or PbI_2−2DMSO + FAI, the kinetic difference of α-$FAPbI_3$ formation can be further reflected and compared in α-$FAPbI_3$ film quality at a close thermodynamic temperature. Herein, 2-methoxyethanol (2ME; DN* = 0.51, β = 0.62), with a weaker binding force in $FAPbI_3$ than DMF (DN* = 0.68, β = 0.69), was chosen as a dispersion cosolvent to disperse (FA···NMP)PbI_3 and PbI_2−2DMSO (with FAI addition) intermediates and to assist the growth of α-$FAPbI_3$ films by a vacuum-flash-assisted blade-coating technology (Figure S15a). Surface and bulk statuses of both films were systematically studied to gain insight into their quality. The (FA···NMP)PbI_3 intermediate film after vacuum flashing exhibited a larger grain size (Figure S15b,c) and higher crystallinity (Figure S15d,e) than PbI_2−2DMSO + FAI. After annealing, both films also exhibited increased grain sizes (Figure S15f,g). Note that, with heating of the (FA···NMP)PbI_3 film at 90 °C or upon treating it with ethyl acetate, the black α-$FAPbI_3$ film formed in a short time (Videos S1 and S2) with a tiny amount of δ-$FAPbI_3$. By contrast, the PbI_2−2DMSO (with FAI addition) intermediate film upon heating at 100 °C or treating by ethyl acetate was transferred to tiny α-$FAPbI_3$ accompanied by major δ-$FAPbI_3$ (Figure S15h,i). The difference of α-$FAPbI_3$ formation between powders and films might be due to the restricted kinetic behavior from the inevitable stress between the substrate and as-deposited film. A small dose of Cs^+ and

https://doi.org/10.1021/acscentsci.2c00385
ACS Cent. Sci. 2022, 8, 1008−1016

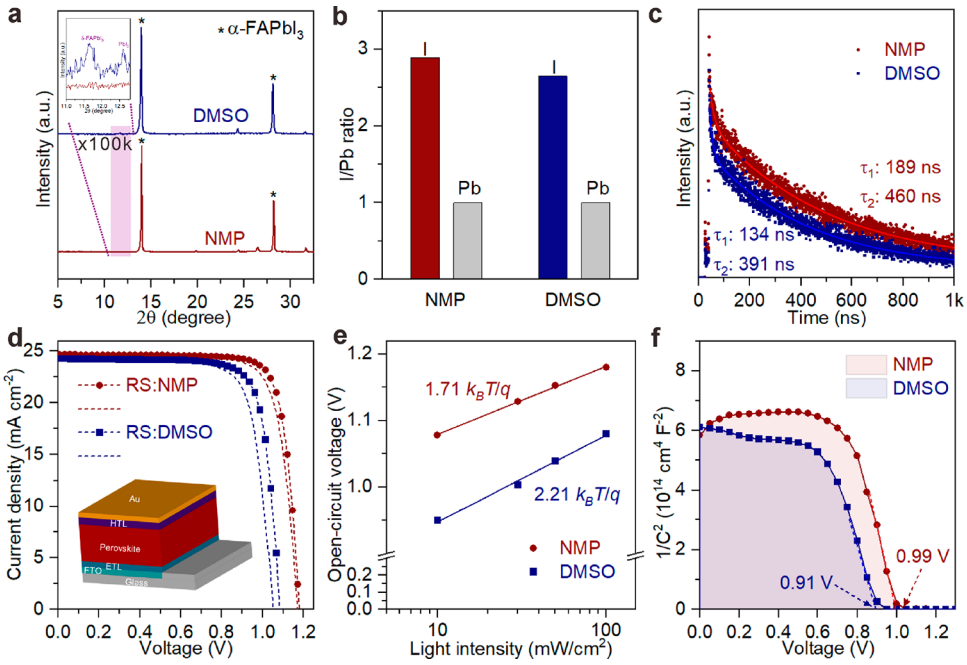

Figure 3. Performance evaluation of $FAPbI_3$-based films prepared from different intermediates and corresponding PSCs. Quality assessments of $FAPbI_3$-based films by (a) XRD patterns, (b) I/Pb relative mole ratio on the perovskite surface from XPS, and (c) TRPL measurements. (d) $J-V$ characteristics of PSCs. (e) Open-circuit voltage as a function of light intensity. The linear plots are fitted by the equation $V_{OC} = n(k_BT/q)$ ln(light intensity) + A (n, ideal factor; k_B, Boltzmann constant; T, absolute temperature; q, elementary charge; A, constant). (f) Mott−Schottky analysis of PSCs from different intermediate films.

$PbCl_2$ additives was introduced to eliminate δ-$FAPbI_3$ and improve film quality (Figure S16a,b). The additive-contained $FAPbI_3$-based film from (FA···NMP)PbI_3 heated at 90 °C (denoted as NMP-film) showed smaller roughness than that from PbI_2−2DMSO (with FAI addition) heated at 100 °C (denoted as DMSO-film; Figure S16c,d). The appearance of minor undesirable δ-$FAPbI_3$ and PbI_2 phase was still observed in the DMSO-film but not in the NMP-film (Figure 3a). X-ray photoelectron spectra (XPS) from the integral area of Pb 4f and I 3d peaks (Figure 3b and Figure S16g,h) reflect that the NMP-film has an obviously higher I/Pb mole ratio than the DMSO-film, proving the fewer iodide vacancies from NMP-film. In addition, the improved surface potential value of the NMP-film (Figure S16e,f) indicates the increased Fermi level of its surface, benefiting from decreased hole traps at crystal boundaries.[51] These features facilitate the efficient hole transport within the NMP-films, confirmed by their longer carrier lifetime and higher fluorescence intensity (Figure 3c and Figure S16i,j). The differentiated quality of α-$FAPbI_3$ film could be attributed to different kinetic behaviors of α-$FAPbI_3$ formation.

Both the NMP-films and DMSO-films were assembled into complete PSCs with a configuration of FTO/ETL/perovskite/HTL/Au. The current density−voltage ($J-V$) characteristics (Figure 3d) show that the PSCs from the NMP-films (abbreviated as NMP-PSCs) achieved an optimized power conversion efficiency (PCE) of 23.43% in reverse scan conditions (RS) and 22.47% in forward scan conditions (FS), superior to the devices based on the DMSO-films (abbreviated as DMSO-PSCs, with an optimized PCE of 20.57% in RS and 19.41% in FS; summarized in Table S7). Reasonably, the α-$FAPbI_3$ film from the PbI_2−2DMSO + FAI route showed better quality and performance than the one directly converted from δ-$FAPbI_3$ film via annealing at 150 °C (Figure S17). The nonradiative recombination in PSCs was compared by the plots of the light intensity-dependent V_{OC} (0.1 sun ≤ light intensity ≤ 1 sun). The lower linear slope of the NMP-PSC ($1.71k_BT/q$) than that of the DMSO-PSC ($2.21k_BT/q$) illustrates that the trap-induced nonradiative recombination process is effectively suppressed within the NMP-PSC (Figure 3e), in good agreement with results of the space-charge-limited current (SCLC) analysis as shown in Figure S18a.[52] Mott−Schottky plots (Figure 3f) intuitively explicate an improved flat band potential in the NMP-PSC. A dark current test (Figure S18b) also demonstrates that the leakage current of the NMP-PSC was of one order magnitude lower than that of the DMSO-PSC, and the photocurrent densities calculated from the incident photon-to-electron conversion efficiency (IPCE) spectra (Figure S18c) were 24.0 and 23.8 mA cm^{-2} for NMP- and DMSO-PSCs, respectively. All of these improved parameters are attributed to the formation of high-quality and defect-less films. The unencapsulated NMP-PSC exhibited outstanding stability (Figure S18d) within 1000 s under continuous steady-state output (~50 °C and ~50% RH), superior to the DMSO-PSC. Twenty individuals were fabricated and displayed relatively little error with 23.12 ± 0.21% and 20.28 ± 0.26% from NMP- and DMSO-PSCs (Figure S18e), respectively. Also, PSCs prepared from (FA···2DMF)PbI_3, (FA···0.5DMA)PbI_3, and (FA···2.5DMI)PbI_3 intermediate films exhibited a superior performance to the DMSO one (Figure S18f). In summary, the superior PSC performance from as-guided (FA···OXR)PbI_3 demonstrates the importance of the solvent gaming chemistry of halide perovskite intermediates in solar cells.

The defect-less $FAPbI_3$-based films from (FA···OXR)PbI_3 are available for the fabrication and stability assessment of large-scale modules. The smooth NMP-films (6 × 6 cm^2) were readily prepared by blade coating in an ambient atmosphere,

https://doi.org/10.1021/acscentsci.2c00385
ACS Cent. Sci. 2022, 8, 1008−1016

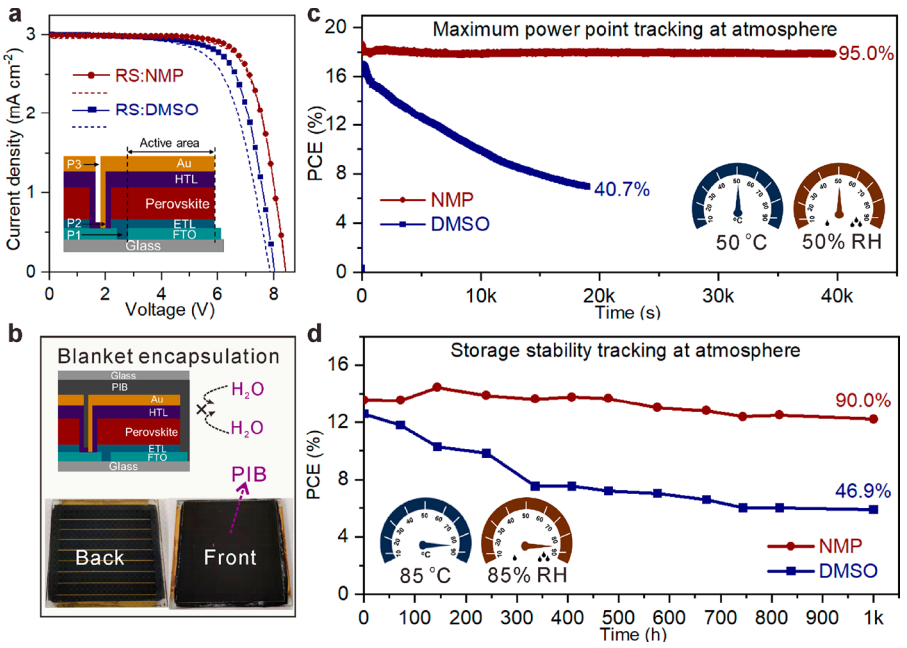

Figure 4. Stability assessment of $FAPbI_3$-based modules with different perovskite films. (a) *J*−*V* of unencapsulated modules. (b) Photographs of an encapsulated module with PIB used as the encapsulant. (c) Maximum power point tracking of modules in an ambient atmosphere (50 °C and 50% RH). (d) Storage stability tracking of encapsulated modules under harsh hydrothermal conditions (85 °C and 85% RH).

and an optimized structure of the series connection was designed for large-scale modules (Figure S19a,b). The best NMP-module (18 cm^2 aperture area) with Spiro-OMeTAD as HTL exhibited a PCE of 18.55% in RS and 18.23% in FS (Figure 4a), ahead of the DMSO-module (Table S8). The larger scale of perovskite films and modules, the more defects influencing the modules' stability. The protected NMP-module (Figure 4b), adapting a polyisobutylene (PIB)-based blanket encapsulation strategy,[53] showed a favorable continuous steady-state output (maintaining 95.0% of initial PCE) upon maximum power point tracking within 40 000 s (under 1 sun condition in an ambient atmosphere, ∼50 °C and ∼50% RH). In contrast, the PCE of the DMSO-module decreased to 40.7% within 20 000 s (Figure 4c). To further improve the modules' stability under harsh aging conditions, the unstable Spiro-OMeTAD was replaced by nickel phthalocyanine (NiPc) with high thermal stability.[54] An aging operation following the ISOS-O standard at 85 °C and 85% RH in the dark state (Figure 4d) was adapted to distinguish the stability difference.[55] While the NMP-module maintained 90.0% of the initial PCE after 1000 h under the harsh damp-heat environment, the DMSO-module fell to 46.9% of the initial PCE. The higher stability of NMP-modules was also demonstrated under the maximum power point at harsh conditions (85 °C and 50% RH; Figure S19c). The enhanced stability of modules from defect-less NMP-films can be attributed to the suppressed vacancy-assisted migration of iodide ions.[56,57]

CONCLUSION

In brief, the disclosed solvent gaming chemistry behind halide perovskite intermediates sequentially clarifies the chemical origin of $FAPbI_3$-based intermediate structures, structural evolutions from solvent-contained intermediates to perovskites, and low-temperature preparation of defect-less films for high-performance devices. It is expected that the exploited solvent gaming chemistry can guide the predictive selection of intermediate structures and designable thermodynamic and kinetic regulation of perovskite formation, and be applied to other solution-processed perovskite systems, such as $CsPbI_3$, Sn-based, or two-dimensional perovskites for different applications.

ASSOCIATED CONTENT

Supporting Information

The Supporting Information is available free of charge at https://pubs.acs.org/doi/10.1021/acscentsci.2c00385.

X-ray data for PbI_2−OXR (CCDC numbers): PbI_2−2DESO (2104894), PbI_2−DMPU (2104895), PbI_2−2DMSO (2104896); X-ray data for (FA···OXR)PbI_3 (CCDC numbers): (FA···0.5DMA)PbI_3 (2104889), (FA···2DMF)PbI_3 (2104890), (FA···2.5DMI)PbI_3 (2104891), (FA···HMPA)PbI_3 (2104892), and (FA···NMP)PbI_3 (2104893); additional experimental details, methods, materials, and photovoltaic performances of the devices (PDF)

Video S1: Heating the (FA···NMP)PbI_3 and PbI_2-2DMSO+FAI films at 90 °C and 100 °C (MP4)

Video S2: Soaking the (FA···NMP)PbI_3 and PbI_2-2DMSO+FAI films by ethyl acetate at room temperature (MP4)

Transparent Peer Review report available (PDF)

AUTHOR INFORMATION

Corresponding Authors

Binghui Wu − *State Key Laboratory for Physical Chemistry of Solid Surfaces, Collaborative Innovation Center of Chemistry for Energy Materials, National & Local Joint Engineering Research Center of Preparation Technology of Nanomaterials, College of Chemistry and Chemical Engineering, Pen-Tung Sah Institute of Micro-Nano Science and Technology, Xiamen University, Xiamen 361005, China; Innovation Laboratory for Sciences and Technologies of*

https://doi.org/10.1021/acscentsci.2c00385
ACS Cent. Sci. 2022, 8, 1008−1016

*Energy Materials of Fujian Province (IKKEM), Xiamen 361102, China; orcid.org/0000-0003-4015-9991; Email: binghuiwu@xmu.edu.cn

Nanfeng Zheng − *State Key Laboratory for Physical Chemistry of Solid Surfaces, Collaborative Innovation Center of Chemistry for Energy Materials, National & Local Joint Engineering Research Center of Preparation Technology of Nanomaterials, College of Chemistry and Chemical Engineering, Pen-Tung Sah Institute of Micro-Nano Science and Technology, Xiamen University, Xiamen 361005, China; Innovation Laboratory for Sciences and Technologies of Energy Materials of Fujian Province (IKKEM), Xiamen 361102, China; orcid.org/0000-0001-9879-4790; Email: nfzheng@xmu.edu.cn

Authors

Xiaofeng Huang − *State Key Laboratory for Physical Chemistry of Solid Surfaces, Collaborative Innovation Center of Chemistry for Energy Materials, National & Local Joint Engineering Research Center of Preparation Technology of Nanomaterials, College of Chemistry and Chemical Engineering, Pen-Tung Sah Institute of Micro-Nano Science and Technology, Xiamen University, Xiamen 361005, China*

Guocheng Deng − *State Key Laboratory for Physical Chemistry of Solid Surfaces, Collaborative Innovation Center of Chemistry for Energy Materials, National & Local Joint Engineering Research Center of Preparation Technology of Nanomaterials, College of Chemistry and Chemical Engineering, Pen-Tung Sah Institute of Micro-Nano Science and Technology, Xiamen University, Xiamen 361005, China*

Shaoqi Zhan − *Department of Chemistry−BMC, Uppsala University, S-751 23 Uppsala, Sweden*

Fang Cao − *State Key Laboratory for Physical Chemistry of Solid Surfaces, Collaborative Innovation Center of Chemistry for Energy Materials, National & Local Joint Engineering Research Center of Preparation Technology of Nanomaterials, College of Chemistry and Chemical Engineering, Pen-Tung Sah Institute of Micro-Nano Science and Technology, Xiamen University, Xiamen 361005, China*

Fangwen Cheng − *State Key Laboratory for Physical Chemistry of Solid Surfaces, Collaborative Innovation Center of Chemistry for Energy Materials, National & Local Joint Engineering Research Center of Preparation Technology of Nanomaterials, College of Chemistry and Chemical Engineering, Pen-Tung Sah Institute of Micro-Nano Science and Technology, Xiamen University, Xiamen 361005, China*

Jun Yin − *State Key Laboratory for Physical Chemistry of Solid Surfaces, Collaborative Innovation Center of Chemistry for Energy Materials, National & Local Joint Engineering Research Center of Preparation Technology of Nanomaterials, College of Chemistry and Chemical Engineering, Pen-Tung Sah Institute of Micro-Nano Science and Technology, Xiamen University, Xiamen 361005, China; Innovation Laboratory for Sciences and Technologies of Energy Materials of Fujian Province (IKKEM), Xiamen 361102, China; orcid.org/0000-0003-4551-3515

Jing Li − *State Key Laboratory for Physical Chemistry of Solid Surfaces, Collaborative Innovation Center of Chemistry for Energy Materials, National & Local Joint Engineering Research Center of Preparation Technology of Nanomaterials, College of Chemistry and Chemical Engineering, Pen-Tung Sah Institute of Micro-Nano Science and Technology, Xiamen University, Xiamen 361005, China; Innovation Laboratory for Sciences and Technologies of Energy Materials of Fujian Province (IKKEM), Xiamen 361102, China; orcid.org/0000-0003-4814-6896

Complete contact information is available at: https://pubs.acs.org/10.1021/acscentsci.2c00385

Author Contributions

[‖]X. Huang, G. Deng, and S. Zhan contributed equally to this work. X. Huang conceived the study, grew all of the crystals, fabricated all of the devices, conducted the relevant measurements, and wrote the first draft of the manuscript. B. Wu and N. Zheng supervised the project, proposed experiments, and wrote the final version of the manuscript. G. Deng resolved the single crystals. S. Zhan carried out the DFT calculations. F. Cao, F. Cheng, J. Yin, and J. Li coordinated the whole project. All authors analyzed the data and contributed to the discussions. We also thank Dr. Xijun Wang, Dr. Zi'ang Nan, and Qi Liu for useful discussions.

Notes

The authors declare the following competing financial interest(s): We have filed a patent (application No. CN202210799602) related to this work.

■ ACKNOWLEDGMENTS

The authors acknowledge funding support from the National Natural Science Foundation of China (22075238, 21805232, and 21721001), the Natural Science Foundation of Jiangxi Province of China (20192ACBL20047), and Science and Technology Projects of Innovation Laboratory for Sciences and Technologies of Energy Materials of Fujian Province (IKKEM, RD2020020101).

■ REFERENCES

(1) Barwick, V. J. Strategies for solvent selection - A literature review. *Trends Anal. Chem.* **1997**, *16*, 293−309.

(2) Reichardt, C. Polarity of ionic liquids determined empirically by means of solvatochromic pyridinium N-phenolate betaine dyes. *Green Chem.* **2005**, *7*, 339−351.

(3) Wang, X. P.; Chen, W. M.; Qi, H.; Li, X. Y.; Rajnak, C.; Feng, Z. Y.; Kurmoo, M.; Boca, R.; Jia, C. J.; Tung, C. H.; et al. Solvent-controlled phase transition of a Co(II)-organic framework: from achiral to chiral and two to three dimensions. *Chem. Eur. J.* **2017**, *23*, 7990−7996.

(4) Adams, J. S.; Chemburkar, A.; Priyadarshini, P.; Ricciardulli, T.; Lu, Y.; Maliekkal, V.; Sampath, A.; Winikoff, S.; Karim, A. M.; Neurock, M.; et al. Solvent molecules form surface redox mediators in situ and cocatalyze O_2 reduction on Pd. *Science* **2021**, *371*, 626−632.

(5) Orozco, M.; Luque, F. J. Theoretical methods for the description of the solvent effect in biomolecular systems. *Chem. Rev.* **2000**, *100*, 4187−4226.

(6) Holoubek, J.; Liu, H.; Wu, Z.; Yin, Y.; Xing, X.; Cai, G.; Yu, S.; Zhou, H.; Pascal, T. A.; Chen, Z.; et al. Tailoring electrolyte solvation for Li metal batteries cycled at ultra-low temperature. *Nat. Energy* **2021**, *2021*, 303−313.

(7) Fan, X.; Wang, C. High-voltage liquid electrolytes for Li batteries: progress and perspectives. *Chem. Soc. Rev.* **2021**, *50*, 10486−10566.

(8) Yan, K. Y.; Long, M. Z.; Zhang, T. K.; Wei, Z. H.; Chen, H. N.; Yang, S. H.; Xu, J. B. Hybrid halide perovskite solar cell precursors: colloidal chemistry and coordination engineering behind device processing for high efficiency. *J. Am. Chem. Soc.* **2015**, *137*, 4460−4468.

(9) Li, B.; Binks, D.; Cao, G.; Tian, J. Engineering halide perovskite crystals through precursor chemistry. *Small* **2019**, *15*, No. e1903613.

(10) Ahn, N.; Son, D. Y.; Jang, I. H.; Kang, S. M.; Choi, M.; Park, N. G. Highly reproducible perovskite solar cells with average efficiency of 18.3% and best efficiency of 19.7% fabricated via lewis base adduct of lead(II) iodide. *J. Am. Chem. Soc.* **2015**, *137*, 8696−8699.
(11) Yang, W. S.; Noh, J. H.; Jeon, N. J.; Kim, Y. C.; Ryu, S.; Seo, J.; Seok, S. I. High-performance photovoltaic perovskite layers fabricated through intramolecular exchange. *Science* **2015**, *348*, 1234−1237.
(12) Deng, Y.; Van Brackle, C. H.; Dai, X.; Zhao, J.; Chen, B.; Huang, J. Tailoring solvent coordination for high-speed, room-temperature blading of perovskite photovoltaic films. *Sci. Adv.* **2019**, *5*, No. eaax7537.
(13) Li, D.; Shi, J.; Xu, Y.; Luo, Y.; Wu, H.; Meng, Q. Inorganic-organic halide perovskites for new photovoltaic technology. *Natl. Sci. Rev.* **2018**, *5*, 559−576.
(14) Jeon, N. J.; Noh, J. H.; Kim, Y. C.; Yang, W. S.; Ryu, S.; Seok, S. I. Solvent engineering for high-performance inorganic-organic hybrid perovskite solar cells. *Nat. Mater.* **2014**, *13*, 897−903.
(15) Xiao, M.; Huang, F.; Huang, W.; Dkhissi, Y.; Zhu, Y.; Etheridge, J.; Gray-Weale, A.; Bach, U.; Cheng, Y. B.; Spiccia, L. A fast deposition-crystallization procedure for highly efficient lead iodide perovskite thin-film solar cells. *Angew. Chem. Int. Ed* **2014**, *53*, 9898−9903.
(16) Bu, T.; Li, J.; Li, H.; Tian, C.; Su, J.; Tong, G.; Ono, L. K.; Wang, C.; Lin, Z.; Chai, N.; et al. Lead halide-templated crystallization of methylamine-free perovskite for efficient photovoltaic modules. *Science* **2021**, *372*, 1327−1332.
(17) Chen, S.; Dai, X.; Xu, S.; Jiao, H.; Zhao, L.; Huang, J. Stabilizing perovskite-substrate interfaces for high-performance perovskite modules. *Science* **2021**, *373*, 902−907.
(18) Cao, J.; Jing, X.; Yan, J.; Hu, C.; Chen, R.; Yin, J.; Li, J.; Zheng, N. Identifying the molecular structures of intermediates for optimizing the fabrication of high-quality perovskite films. *J. Am. Chem. Soc.* **2016**, *138*, 9919−9926.
(19) Cheng, F. W.; Jing, X. J.; Chen, R. H.; Cao, J.; Yan, J. Z.; Wu, Y. Y. Q.; Huang, X. F.; Wu, B. H.; Zheng, N. F. N-Methyl-2-pyrrolidone as an excellent coordinative additive with a wide operating range for fabricating high-quality perovskite films. *Inorg. Chem. Front* **2019**, *6*, 2458−2463.
(20) Kojima, A.; Teshima, K.; Shirai, Y.; Miyasaka, T. Organometal halide perovskites as visible-light sensitizers for photovoltaic cells. *J. Am. Chem. Soc.* **2009**, *131*, 6050−6051.
(21) Jeong, M.; Choi, I. W.; Go, E. M.; Cho, Y.; Kim, M.; Lee, B.; Jeong, S.; Jo, Y.; Choi, H. W.; Lee, J.; et al. Stable perovskite solar cells with efficiency exceeding 24.8% and 0.3-V voltage loss. *Science* **2020**, *369*, 1615−1620.
(22) Yoo, J. J.; Seo, G.; Chua, M. R.; Park, T. G.; Lu, Y.; Rotermund, F.; Kim, Y.-K.; Moon, C. S.; Jeon, N. J.; Correa-Baena, J.-P.; et al. Efficient perovskite solar cells via improved carrier management. *Nature* **2021**, *590*, 587−593.
(23) Min, H.; Kim, M.; Lee, S. U.; Kim, H.; Kim, G.; Choi, K.; Lee, J. H.; Seok, S. I. Efficient, stable solar cells by using inherent bandgap of alpha-phase formamidinium lead iodide. *Science* **2019**, *366*, 749−753.
(24) Shang, Y.; Liao, Y.; Wei, Q.; Wang, Z.; Xiang, B.; Ke, Y.; Liu, W.; Ning, Z. Highly stable hybrid perovskite light-emitting diodes based on Dion-Jacobson structure. *Sci. Adv.* **2019**, *5*, No. eaaw8072.
(25) Xue, J.; Lee, J.-W.; Dai, Z.; Wang, R.; Nuryyeva, S.; Liao, M. E.; Chang, S.-Y.; Meng, L.; Meng, D.; Sun, P.; et al. Surface ligand management for stable $FAPbI_3$ perovskite quantum dot solar cells. *Joule* **2018**, *2*, 1866−1878.
(26) Hui, W.; Chao, L.; Lu, H.; Xia, F.; Wei, Q.; Su, Z.; Niu, T.; Tao, L.; Du, B.; Li, D.; et al. Stabilizing black-phase formamidinium perovskite formation at room temperature and high humidity. *Science* **2021**, *371*, 1359−1364.
(27) Li, N.; Niu, X.; Li, L.; Wang, H.; Huang, Z.; Zhang, Y.; Chen, Y.; Zhang, X.; Zhu, C.; Zai, H.; et al. Liquid medium annealing for fabricating durable perovskite solar cells with improved reproducibility. *Science* **2021**, *373*, 561−567.
(28) Jung, M.; Ji, S. G.; Kim, G.; Seok, S. I. Perovskite precursor solution chemistry: from fundamentals to photovoltaic applications. *Chem. Soc. Rev.* **2019**, *48*, 2011−2038.
(29) Romiluyi, O.; Eatmon, Y.; Ni, R.; Rand, B. P.; Clancy, P. The efficacy of Lewis affinity scale metrics to represent solvent interactions with reagent salts in all-inorganic metal halide perovskite solutions. *J. Mater. Chem. A* **2021**, *9*, 13087−13099.
(30) Petrov, A. A.; Fateev, S. A.; Khrustalev, V. N.; Li, Y. M.; Dorovatovskii, P. V.; Zubavichus, Y. V.; Goodilin, E. A.; Tarasov, A. B. Formamidinium haloplumbate intermediates: the missing link in a chain of hybrid perovskites crystallization. *Chem. Mater.* **2020**, *32*, 7739−7745.
(31) Han, Q.; Bae, S. H.; Sun, P.; Hsieh, Y. T.; Yang, Y. M.; Rim, Y. S.; Zhao, H.; Chen, Q.; Shi, W.; Li, G.; et al. Single crystal formamidinium lead iodide ($FAPbI_3$): insight into the structural, optical, and electrical properties. *Adv. Mater.* **2016**, *28*, 2253−2258.
(32) Frost, J. M.; Butler, K. T.; Brivio, F.; Hendon, C. H.; van Schilfgaarde, M.; Walsh, A. Atomistic origins of high-performance in hybrid halide perovskite solar cells. *Nano Lett.* **2014**, *14*, 2584−2590.
(33) Chen, T.; Foley, B. J.; Park, C.; Brown, C. M.; Harriger, L. W.; Lee, J.; Ruff, J.; Yoon, M.; Choi, J. J.; Lee, S. H. Entropy-driven structural transition and kinetic trapping in formamidinium lead iodide perovskite. *Sci. Adv.* **2016**, *2*, No. e1601650.
(34) Zhang, H.; Cheng, J.; Li, D.; Lin, F.; Mao, J.; Liang, C.; Jen, A. K.; Gratzel, M.; Choy, W. C. Toward all room-temperature, solution-processed, high-performance planar perovskite solar cells: a new scheme of pyridine-promoted perovskite formation. *Adv. Mater.* **2017**, *29*, No. 1604695.
(35) Barrit, D.; Cheng, P.; Darabi, K.; Tang, M. C.; Smilgies, D. M.; Liu, S.; Anthopoulos, T. D.; Zhao, K.; Amassian, A. Room-temperature partial conversion of α-$FAPbI_3$ perovskite phase via PbI_2 solvation enables high-performance solar cells. *Adv. Funct. Mater.* **2020**, *30*, No. 1907442.
(36) Huang, X.; Chen, R.; Deng, G.; Han, F.; Ruan, P.; Cheng, F.; Yin, J.; Wu, B.; Zheng, N. Methylamine-dimer-induced phase transition toward $MAPbI_3$ films and high-efficiency perovskite solar modules. *J. Am. Chem. Soc.* **2020**, *142*, 6149−6157.
(37) Zhou, Z.; Wang, Z.; Zhou, Y.; Pang, S.; Wang, D.; Xu, H.; Liu, Z.; Padture, N. P.; Cui, G. Methylamine-gas-induced defect-healing behavior of $CH_3NH_3PbI_3$ thin films for perovskite solar cells. *Angew. Chem. Int. Ed* **2015**, *54*, 9705−9709.
(38) Cheng, F.; Zhan, S.; Dai, X.; Huang, X.; Wu, B.; Zheng, N. Low-temperature fabrication of phase-pure α-$FAPbI_3$ films by cation exchange from two-dimensional perovskites for solar cell applications. *Energy Fuels* **2021**, *35*, 19035−19044.
(39) Xiang, W.; Zhang, J.; Liu, S.; Albrecht, S.; Hagfeldt, A.; Wang, Z. Intermediate phase engineering of halide perovskites for photovoltaics. *Joule* **2022**, *6*, 315−339.
(40) Huang, X.; Cheng, F.; Wu, B.; Zheng, N. Intermediate Chemistry of Halide Perovskites: Origin, Evolution, and Application. *J. Phys. Chem. Lett.* **2022**, *13*, 1765−1776.
(41) Gutmann, V. Empirical parameters for donor and acceptor properties of solvents. *Electrochim. Acta* **1976**, *21*, 661−670.
(42) Johnson, L.; Li, C.; Liu, Z.; Chen, Y.; Freunberger, S. A.; Ashok, P. C.; Praveen, B. B.; Dholakia, K.; Tarascon, J. M.; Bruce, P. G. The role of LiO_2 solubility in O_2 reduction in aprotic solvents and its consequences for Li-O_2 batteries. *Nat. Chem.* **2014**, *6*, 1091−1099.
(43) Taft, R. W.; Gurka, D.; Joris, L.; Schleyer, P. v. R.; Rakshys, J. W. Studies of hydrogen-bonded complex formation with p-fluorophenol. V. Linear free energy relationships with OH reference acids. *J. Am. Chem. Soc.* **1969**, *91*, 4801−4808.
(44) Xia, Y.; Song, Z.; Tan, Z.; Xue, T.; Wei, S.; Zhu, L.; Yang, Y.; Fu, H.; Jiang, Y.; Lin, Y.; et al. Accelerated polymerization of N-carboxyanhydrides catalyzed by crown ether. *Nat. Commun.* **2021**, *12*, No. 732.
(45) Hamill, J. C.; Schwartz, J.; Loo, Y. L. Influence of solvent coordination on hybrid organic−inorganic perovskite formation. *ACS Energy Lett.* **2018**, *3*, 92−97.

https://doi.org/10.1021/acscentsci.2c00385
ACS Cent. Sci. 2022, 8, 1008−1016

(46) Chao, L.; Niu, T.; Gao, W.; Ran, C.; Song, L.; Chen, Y.; Huang, W. Solvent engineering of the precursor solution toward large-area production of perovskite solar cells. *Adv. Mater.* **2021**, *33*, No. 2005410.
(47) Ahlawat, P.; Hinderhofer, A.; Alharbi, E. A.; Lu, H.; Ummadisingu, A.; Niu, H.; Invernizzi, M.; Zakeeruddin, S. M.; Dar, M. I.; Schreiber, F.; et al. A combined molecular dynamics and experimental study of two-step process enabling low-temperature formation of phase-pure alpha-$FAPbI_3$. *Sci. Adv.* **2021**, *7*, No. eabe3326.
(48) Du, T.; Macdonald, T. J.; Yang, R. X.; Li, M.; Jiang, Z.; Mohan, L.; Xu, W.; Su, Z.; Gao, X.; Whiteley, R. Additive-free, low-temperature crystallization of stable alpha-$FAPbI_3$ perovskite. *Adv. Mater.* **2021**, *34* (9), No. 2107850.
(49) Zhang, F.; Huang, S.; Wang, P.; Chen, X.; Zhao, S.; Dong, Y.; Zhong, H. Colloidal synthesis of air-stable $CH_3NH_3PbI_3$ quantum dots by gaining chemical insight into the solvent effects. *Chem. Mater.* **2017**, *29*, 3793−3799.
(50) Zhang, X.; Han, D.; Wang, C.; Muhammad, I.; Zhang, F.; Shmshad, A.; Xue, X.; Ji, W.; Chang, S.; Zhong, H. Highly efficient light emitting diodes based on in situ fabricated $FAPbI_3$ nanocrystals: solvent effects of on-chip crystallization. *Adv. Opt. Mater.* **2019**, *7*, No. 1900774.
(51) Chen, R.; Wu, Y.; Wang, Y.; Xu, R.; He, R.; Fan, Y.; Huang, X.; Yin, J.; Wu, B.; Li, J.; et al. Crown ether-assisted growth and scaling up of $FACsPbI_3$ films for efficient and stable perovskite solar modules. *Adv. Funct. Mater.* **2021**, *31*, No. 2008760.
(52) Jeong, M. J.; Yeom, K. M.; Kim, S. J.; Jung, E. H.; Noh, J. H. Spontaneous interface engineering for dopant-free poly(3-hexylthiophene) perovskite solar cells with efficiency over 24%. *Energy Environ. Sci.* **2021**, *14*, 2419−2428.
(53) Shi, L.; Bucknall, M. P.; Young, T. L.; Zhang, M.; Hu, L.; Bing, J. M.; Lee, D. S.; Kim, J.; Wu, T.; Takamure, N.; et al. Gas chromatography-mass spectrometry analyses of encapsulated stable perovskite solar cells. *Science* **2020**, *368*, No. eaba2412.
(54) Yu, Z.; Wang, L.; Mu, X.; Chen, C. C.; Wu, Y.; Cao, J.; Tang, Y. Intramolecular electric field construction in metal phthalocyanine as dopant-free hole transporting material for stable perovskite solar cells with > 21% efficiency. *Angew. Chem. Int. Ed* **2021**, *60*, 6294−6299.
(55) Khenkin, M. V.; Katz, E. A.; Abate, A.; Bardizza, G.; Berry, J. J.; Brabec, C.; Brunetti, F.; Bulović, V.; Burlingame, Q.; Di Carlo, A.; et al. Consensus statement for stability assessment and reporting for perovskite photovoltaics based on ISOS procedures. *Nat. Energy* **2020**, *5*, 35−49.
(56) Eames, C.; Frost, J. M.; Barnes, P. R.; O'Regan, B. C.; Walsh, A.; Islam, M. S. Ionic transport in hybrid lead iodide perovskite solar cells. *Nat. Commun.* **2015**, *6*, No. 7497.
(57) Deng, Y. H.; Xu, S.; Chen, S. S.; Xiao, X.; Zhao, J. J.; Huang, J. S. Defect compensation in formamidinium-caesium perovskites for highly efficient solar mini-modules with improved photostability. *Nat. Energy* **2021**, *6*, 633−641.

https://doi.org/10.1021/acscentsci.2c00385
ACS Cent. Sci. 2022, 8, 1008−1016